

Project No: 603502

DACCIWA

"Dynamics-aerosol-chemistry-cloud interactions in West Africa"

Deliverable

D° 5.1

Climatology for cloud, aerosol and radiative fluxes

Due date of deliverable: 31/07/2015

Completion date of deliverable: 03/08/2015

Start date of DACCIWA project: 1st December 2013 **Project duration:** 60 months

Version: [V1.0]

File name: [D°_5.1_DACCIWA_v.1.0pdf]

Work Package Number: 5

Task Number: 5.1

Responsible partner for deliverable: UREAD

Contributing partners:

Project coordinator name: Prof. Dr. Peter Knippertz

Project coordinator organisation name: Karlsruher Institut für Technologie

The DACCIWA Project is funded by the European Union's Seventh Framework Programme for research, technological development and demonstration under grant agreement no 603502.

Dissemination level		
PU	Public	x
PP	Restricted to other programme participants (including the Commission Services)	
RE	Restricted to a group specified by the consortium (including the Commission Services)	
CO	Confidential, only for members of the consortium (including the Commission Services)	

Nature of Deliverable		
R	Report	x
P	Prototype	
D	Demonstrator	
O	Other	

Copyright

This Document has been created within the FP7 project DACCIWA. The utilization and release of this document is subject to the conditions of the contract within the 7th EU Framework Programme. Project reference is FP7-ENV-2013-603502.

DOCUMENT INFO**Authors**

Author	Beneficiary Short Name	E-Mail
Thorwald Stein	UREAD	t.h.m.stein@reading.ac.uk
Peter Hill	UREAD	p.g.hill@reading.ac.uk
Richard Allan	UREAD	r.p.allan@reading.ac.uk
Christine Chiu	UREAD	c.j.chiu@reading.ac.uk

Changes with respect to the DoW

Issue	Comments
-	-

Dissemination and uptake

Target group addressed	Project internal / external
Scientific community	Internal and external

Document Control

Document version #	Date	Changes Made/Comments
v0.1	03/07/2015	First version submitted to DACCIWA partners for comments. Current report misses description of frequency of days (as noted in document).
v0.2	29/07/2015	Revised version after comments P.Knippertz, A.Fink and J. Marsham.
v1.0	03/08/2015	Final version approved by the Steering Committee

Table of Contents

Acronyms.....	5
Abstract	6
1 Introduction	6
2 Data and methods.....	6
2.1 Precipitation (TRMM)	7
2.2 Clouds (CM-SAF, CloudSat, CALIPSO).....	7
2.3 Aerosol (SeaWiFS, MODIS, MISR).....	8
2.4 Radiative fluxes (CERES, GERB).....	9
3 Results.....	10
3.1 Climatological mean (2004-2011)	10
3.1.1 Clouds and precipitation	10
3.1.2 Aerosol	12
3.1.3 Radiative fluxes	13
3.1.4 Moisture budget.....	16
3.2 Diurnal cycle	17
3.2.1 Clouds and precipitation	17
3.2.2 Frequency of cloud occurrence.....	18
3.2.3 Radiative fluxes	19
3.3 Interannual variability	20
3.3.1 Clouds and precipitation	20
3.3.2 Radiative fluxes	22
4 Summary and key findings.....	23
5 References	24

Acronyms

A-Train	“Afternoon” Train, a constellation of polar-orbiting, sun-synchronous satellites, which include CloudSat, CALIPSO, and Aqua (which carries the MODIS and CERES instruments).
CALIPSO	Cloud-Aerosol Lidar and Infrared Pathfinder Satellite Observation, part of the A-Train
CloudSat	Cloud Satellite, part of the A-Train, carries the CloudSat profiling radar.
CM-SAF	EUMETSAT Climate Monitoring Satellite Application Facility
EUMETSAT	European Organisation for the Exploitation of Meteorological Satellites
IR	Infrared
MISR	the Multi-angle Imaging Space Radiometer
MODIS	the Moderate Resolution Imaging Spectroradiometer
OLR	Outgoing Longwave Radiation at top of atmosphere
SeaWiFS	the Sea-Viewing Wide Field-of-View Sensor
SEVIRI	Spinning Enhanced Visible and Infrared Imager
SWA	southern West Africa
TOA	the Top of the Atmosphere
TRMM	Tropical Rainfall Measuring Mission

Abstract

This report provides a multi-year multi-satellite analysis of clouds, aerosol, precipitation and radiative fluxes for the wider southern West Africa region. This provides a climatological context from which to plan and interpret the intensive observations undertaken by DACCIWA and a resource for the project. Multi-year averages and interannual variability of radiative fluxes, cloud fraction and type, aerosol optical depth, and precipitation are constructed over the climatological period (2000-present) using products derived from SEVIRI and GERB (aboard Meteosat), CERES, MODIS, SeaWiFS, and TRMM. These are augmented by reanalyses estimates of moisture fluxes and evaporation from ERA Interim. An integrated representation of radiative processes, including diurnal cycle and trend analyses, is generated for two smaller regions centred on Kumasi (Ghana) and Savé (Benin). Interrelationships between variables are discussed, as well as possible improvements to the low-level cloud climatology using overlap statistics.

1 Introduction

One principal aim of DACCIWA is to advance the scientific understanding of the interactions between emissions (natural and anthropogenic), clouds, radiation, precipitation, and the regional atmospheric circulation for southern West Africa (SWA). These interactions will be monitored and measured extensively during a field campaign planned for June-July 2016. The West African monsoon exhibits a complex spatial structure and strong interannual variability in its onset date and rainfall amounts (Sultan and Janicot, 2003; Liebmann et al. 2012), which in turn may affect cloud cover and synoptic situation observed during the field campaign.

The purpose of this report is therefore to provide the regional and climatological context of several key variables, so that findings from the field campaign may be interpreted with this knowledge in mind. This report focuses on satellite observations, while a separate DACCIWA report will be prepared for surface observations. The climatological period considered runs from 2000-present and is determined by the availability of several state-of-the-art and widely used satellite retrieval products. The satellite-based climatology is complemented by moisture budget calculations from ERA-Interim reanalysis data. This will provide a dynamical regional context of the water cycle.

This report is concluded with a list of key findings from the multi-year multi-satellite analysis.

2 Data and methods

The multi-year climatologies are calculated for the period 2004-2011, to coincide with the availability of CM-SAF products provided by EUMETSAT (see Table 1 for an overview of satellite products and their availability). This period encompasses the availability of GERB measurements and part of the A-Train satellite period (before CloudSat anomalies forced daytime-only observations in October 2011). TRMM measurements are available from 1998-2011, CERES and MODIS are available from the Terra satellite from December 1999 onwards and Aqua satellite from 2002 onwards; data prior to 2004 and after 2011 are used for analysis of inter-annual variability but are excluded from the multi-year climatologies. Results are presented for June and July separately, with the understanding that June covers the monsoon onset period, assuming a mean Sahelian onset date of 24 June (Sultan and Janico, 2003) and during July SWA experiences relatively lower rainfall amounts (Nguyen et al., 2011; Liebmann et al. 2012).

CM-SAF and TRMM products are analysed on a regular $0.25^\circ \times 0.25^\circ$ grid. Maps of monthly means and time-series analysis are averaged over the diurnal cycle. Time series analysis and diurnal

cycles of several variables are provided for two separate 5°x 5° subdomains centred on Kumasi (Ghana) and Savé (Benin) respectively.

Table 1: A summary of satellite datasets used in multi-year analyses. Resolution considers the resolution of the retrieval product considered in this report, “M” indicates that the product concerns a polar-orbiting satellite and only monthly means are considered. Shaded boxes indicate for which years the satellite products are considered.

Data set/ Observable	Resolution	98	99	00	01	02	03	04	05	06	07	08	09	10	11	12	13	14
Cloud																		
CM-SAF	0.027°; 1hr																	
CloudSat	1.5 km; M																	
CALIPSO	1.5 km; M																	
Aerosol																		
MODIS	1°; M																	
SeaWiFS	1°; M																	
MISR	0.5°; M																	
Precipitation																		
TRMM	0.25°; 3hr																	
Radiation																		
CERES	1°; M																	
GERB	0.08°; 15min																	
Multi-year mean																		
Diurnal cycle																		
Inter-annual variability																		

2.1 Precipitation (TRMM)

Rainfall climatology is calculated from the TRMM 3B42 merged microwave-IR rainfall product, which is provided at 0.25°x 0.25° resolution every 3 hours (Huffman et al., 2007).

2.2 Clouds (CM-SAF, CloudSat, CALIPSO)

The CM-SAF data products (EUMETSAT Climate Monitoring Satellite Application Facility, Stengel et al., 2014) are derived every hour from SEVIRI observations at 0.027° resolution. We use cloud-top pressure to define high-level (pressure $p < 350$ hPa), mid-level ($350 < p < 650$ hPa), and low-level ($p > 650$ hPa) clouds. Cloud fractions are calculated for each 0.25°x 0.25° grid box from the number of observations of a certain cloud type, divided by the total number of observations. No consideration of cloud-overlap is taken, so the climatological means for low-level cloud and mid-level cloud are a lower estimate of the true fractions, as these clouds may be obscured by high-level clouds (or mid-level clouds in the case of low-level clouds). It should also be noted that by grouping clouds in these broad categories, we combine clouds with distinctly different physical origins and different diurnal behaviours, such as ultra-low nocturnal clouds (Knippertz et al., 2011), stratus, and cumulus humilis (Andreas Fink, personal communication).

Two main issues affect the CM-SAF cloud-top pressure retrievals. Firstly, the detection of low-level cloud at night relies on the temperature difference between the cloud top and the surface. Such temperature difference may be small at night (especially for ultra-low clouds) and low-level cloud detection is therefore poor. Secondly, around dawn and dusk solar zenith angle effects cause dust and aerosol to be erroneously classed as cloud. This leads to increased low-level cloud detection over the Sahel and Sahara, especially at dusk when mesoscale convection systems may have led to dust uplift during the day.

CloudSat and CALIPSO were launched in June 2006 to join the A-Train constellation of satellites, providing a multi-instrument look at clouds and aerosols. The CloudSat profiling radar and CALIPSO lidar observe the vertical structure of clouds and precipitation, but due to their narrow footprint and their sun-synchronous polar orbit, their use is limited to climatological understanding only, and not for diurnal cycle or trend analysis. In this report, we use only the DARDAR cloud mask from the merged CloudSat-CALIPSO data, from which we calculate overlap statistics to potentially improve the CM-SAF climatology.

2.3 Aerosol (SeaWiFS, MODIS, MISR)

Aerosol optical depths are taken from three sources: SeaWiFS, MODIS, MISR. In all three products, aerosol properties are only retrieved in clear-sky, resulting in little data in the west and east sub-domains, which are very cloudy (see for example Figure 1).

SeaWiFS was launched in August 1997 and produced observations until December 2010. The satellite had a sun-synchronous orbit with an orbital period of 99 minutes, crossing the equator at approximately 12.20 local time. The horizontal resolution is 4.5 km at the centre of the swath. Aerosol properties are produced for 3x3 native SeaWiFS pixels. Independent algorithms are used over ocean (Sayer et al., 2012) and land (Hsu et al., 2013a). We use the combined land and ocean aerosol optical thickness at 550-nm wavelength with a horizontal resolution of 1° from the monthly Level 3 gridded product (Hsu et al., 2013b). This monthly variable in the product is the arithmetic mean of the relevant daily variables, with requirement of at least 3 days of data in the month in order to calculate a mean. Months from different years are weighted equally in the calculation of the climatology, regardless of the number of samples in each month.

We take MODIS observations from both the Terra and Aqua satellites. Both satellites have sun-synchronous orbits; the local equator crossing time during the day is 10.30 for Terra and 13.30 for Aqua. Since aerosol retrievals rely on solar reflectance measurements, retrievals are only available during the day. Three algorithms are used in the MODIS product, depending on surface types such as ocean, dark land surface and bright land surface (i.e. the so-called 'deep blue' algorithm that is also used by SeaWiFS over land). We use the combined dark target and deep blue aerosol optical thickness at 550-nm wavelength variable (Levy et al., 2013), taken from the monthly Level 3 product. Similar to the approach applied in the SeaWiFS dataset, the horizontal resolution is 1°, and equal weighting is applied in the calculation of the climatology.

MISR is an instrument on the Terra satellite (that also carries one of the MODIS instruments). It consists of 9 cameras with an overlapping swath that is 360 km wide with a resolution of 1.1 km. We use the optical depth at 555-nm wavelength, taken from the MISR monthly product (MISR Science Team, 2015). The original resolution is 0.5°. For comparison with SeaWiFS and MODIS this is averaged to 1° resolution with weighting from the number of samples in each 0.5° cell. As for SeaWiFS and MODIS, further averages are calculated without any weighting.

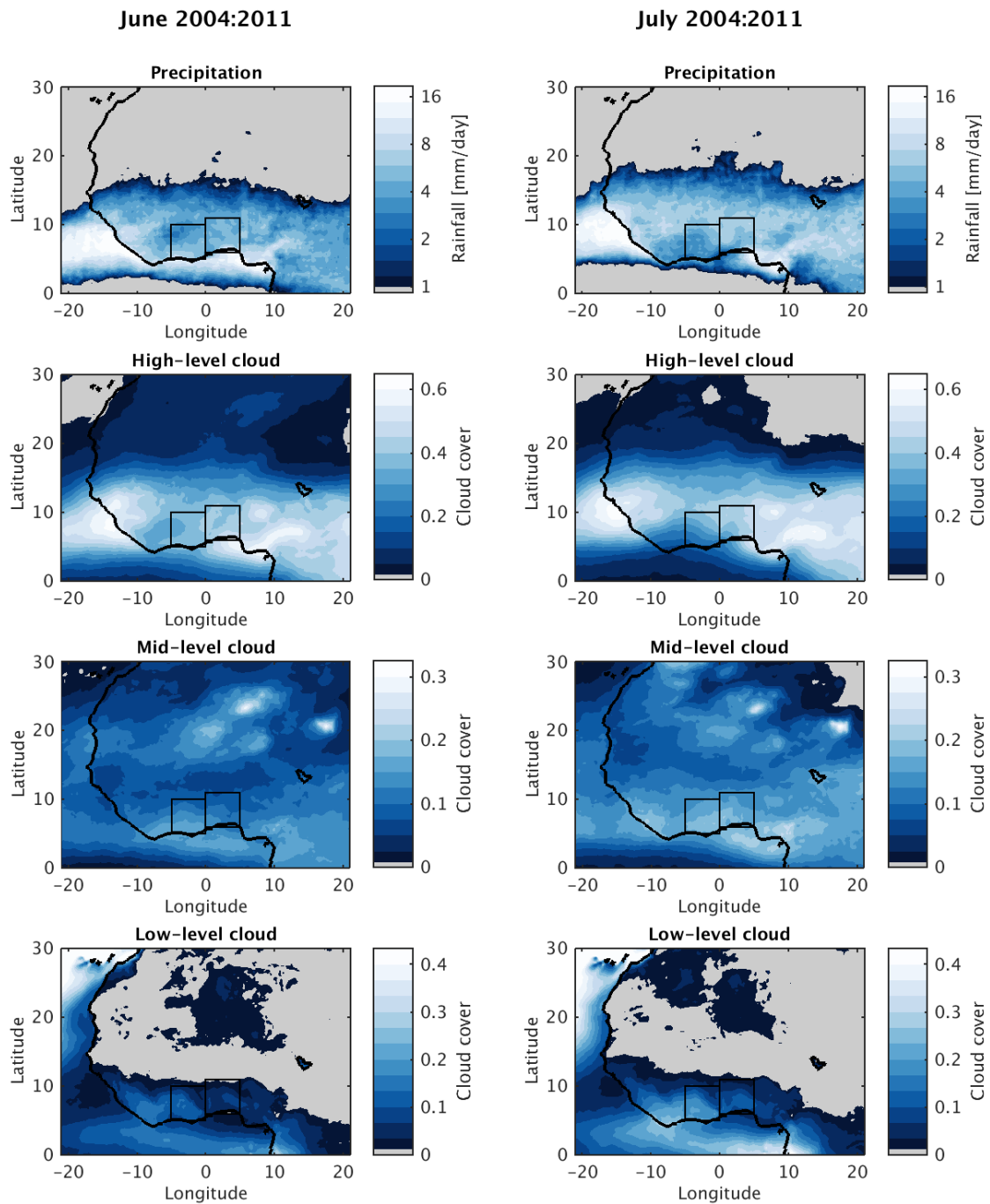


Figure 1. Multi-annual (2004-2011) climatologies of TRMM precipitation (first row) and upper, mid and low-level cloud fraction from CM-SAF (second to fourth rows) for June (left) and July (right). Grey shading indicates rainfall below 1 mm day^{-1} or cloud cover below 0.01. Boxes denote regions in which interannual and diurnal variability are computed.

2.4 Radiative fluxes (CERES, GERB)

The CERES (Clouds and the Earth's Radiant Energy System) surface and TOA (top of atmosphere) observations described in this report are taken from version 2.8 of the CERES EBAF (energy balanced and filled) surface and TOA datasets (CERES Science Team, 2014; CERES Science Team, 2015) respectively. The EBAF products are constrained so that the global net TOA flux is consistent with the best estimate of heat storage in the Earth-atmosphere system ($\sim 0.58 \text{ W m}^{-2}$) (Loeb et al., 2009). The CERES TOA radiance measurements are converted to radiative

fluxes using scene-dependent angular dependence models. However, surface fluxes are computed using observationally-based vertical profiles of clouds and atmospheric composition, constrained to match the TOA radiative fluxes.

The CERES-EBAF datasets provide monthly mean fluxes at a spatial resolution of 1° . The climatology is a simple unweighted mean of the monthly values. The interannual means for each subdomain are simple means of the $5^\circ \times 5^\circ$ CERES monthly values, while the error bars show the standard error calculated from spatial variability.

The GERB instrument (Harries et al., 2005) is a broadband radiometer aboard MeteoSat, which takes radiation measurements at approximately 50 km resolution, every 6 min. The product used in this report is the “Standard High-resolution Image” (DeWitte et al., 2008), in which the data are processed using cloud observations from SEVIRI to convert radiance measurements to radiative fluxes at approximately 10 km resolution, every 15 min. The GERB climatologies are compared against CERES, the latter being preferred for its longer time period. As GERB is geostationary, it allows analysis of the diurnal cycle of radiation, to be discussed alongside the cloud-type cover and rainfall cycles.

3 Results

3.1 Climatological mean (2004-2011)

3.1.1 Clouds and precipitation

Figure 1 shows the mean daily rainfall and fractional high-level, mid-level, and low-level cloud cover for June and July 2004–2011. The patterns for high-level cloud and rainfall are extremely similar, with maxima off the coast of Nigeria and the coast of Guinea in both June and July, and a slight northward progression of the oceanic rain belt (20°W). Over land, maxima of high-level cloud cover and precipitation are evident over the Guinea highlands (10°W , 10°N) and the Cameroon highlands (10°E , 7°N). In June, a minimum of high-level cloud is over Ivory Coast (6°W , 8°N), slightly displaced to the southwest of a rainfall minimum. In July, a rainfall minimum is more widespread along the coast, covering Liberia, Ivory Coast, Ghana, and southern Togo and Benin; this broadly coincides with a minimum in high-level cloud cover.

Mid-level clouds occur throughout West Africa with approximately 5–10% cloud cover and 10–20% along the SWA coast in June and July. The coastal mid-level cloud is more widespread in July, although there is a possible enhancement simply due to less cloud obscured by high-level cloud in July.

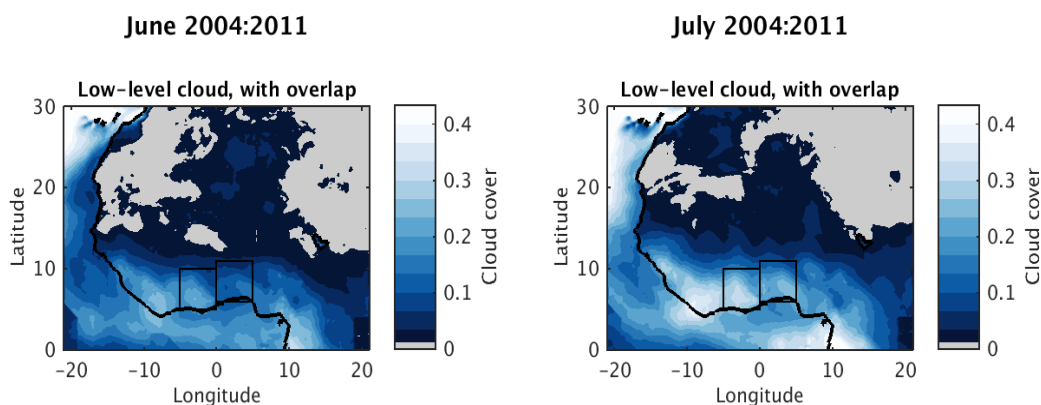


Figure 2. Low-level cloud cover derived from CM-SAF but adjusted with CloudSat-CALIPSO overlap statistics. Left: June, Right: July.

Low-level cloud cover is maximum over the North Atlantic (north of 10°N) and in the Gulf of Guinea, along a band stretching from Equatorial Guinea NE-wards to south of Liberia. Low-level cloud cover in the Gulf of Guinea increases in July. Over land, low-level cloud is confined to SWA (south of 10°N), in a region stretching from western Nigeria to Guinea, and then northwards along the Atlantic coast towards Senegal. Daily mean low-level cloud cover over land is maximum over Ivory Coast, about 10% in June and 20% in July. The continental maxima coincide with reduced high-level cloud cover, again indicating a possible occurrence of low clouds being obscured by high clouds in the satellite view.

We briefly comment on the estimated fraction of low-level cloud obscured in CM-SAF by high-level and mid-level clouds. Using CloudSat-CALIPSO observations, we can estimate the fractional cloud

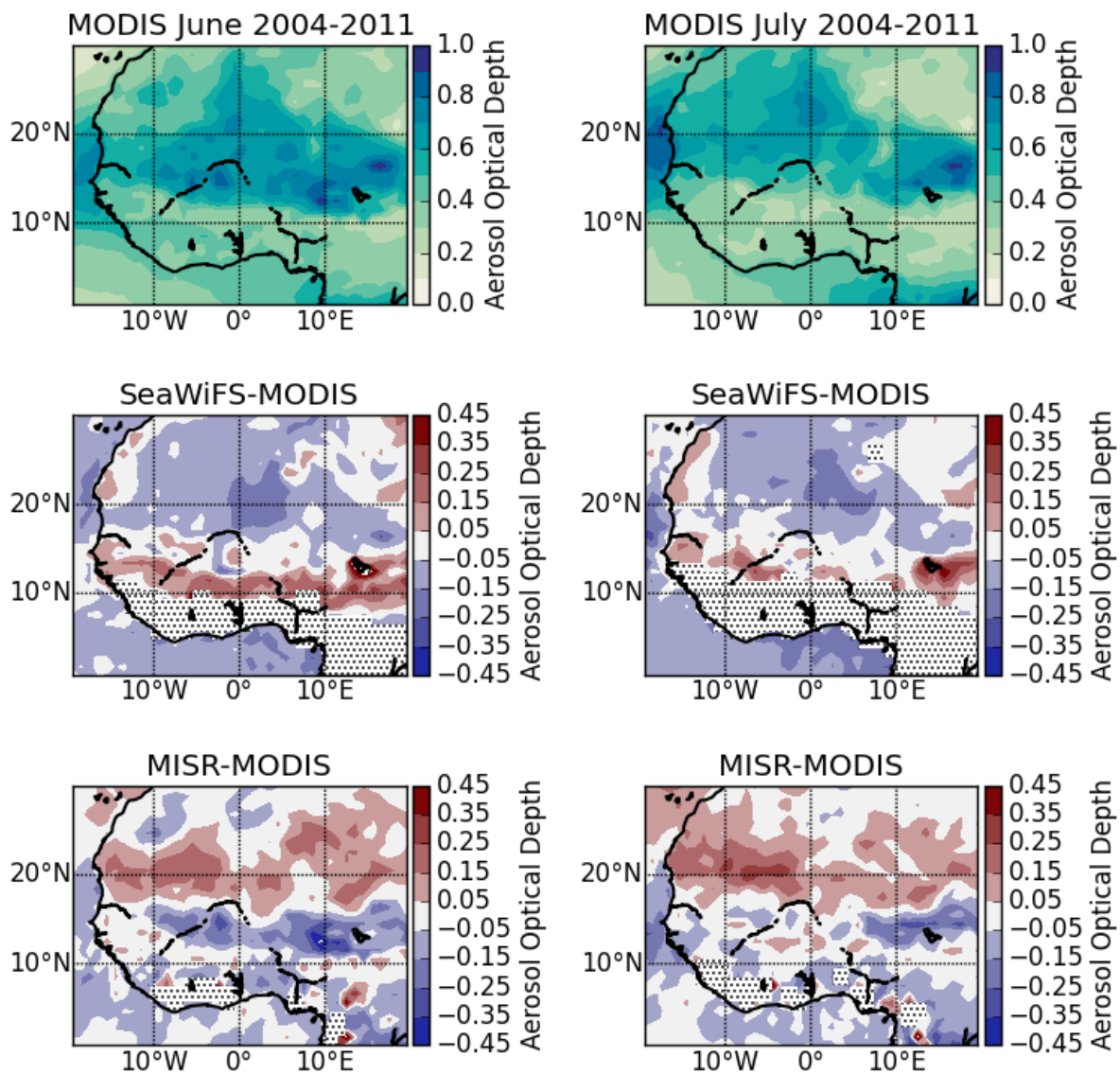


Figure 3. Multi-annual (2004-2011) climatologies of aerosol optical thickness at 550 nm (555 nm for MISR) for June (left) and July (right). Top row shows MODIS AOD from the combined dark target deep blue product. Middle row shows differences between this MODIS AOD and the mean SeaWiFS combined land-ocean AOD (up to 2010). Bottom row shows differences between this MODIS AOD and the mean MISR AOD. Speckling indicates missing data.

cover from low-level clouds, similar to CM-SAF. The cloud-penetrating nature of the radar and lidar allows us to detect a much higher fraction of low-level clouds, which can be compared to the fraction of low-level clouds that have no cloud layer above. Results (not shown) suggest that the actual low-level cloud fraction is about a factor 2–3 greater than the low-level cloud fraction simply derived from CM-SAF. In Fig. 2, we show the CM-SAF low-level cloud cover again, but now adjusted with estimates of multi-layered clouds from CloudSat-CALIPSO. Although the method is still in development, in principal we simply add two fractions to the low-level cloud cover, namely (1) the fraction of low-level cloud under high-level cloud (which is the probability of low-level cloud under high-level cloud times the fraction of high-level cloud) and (2) the fraction of low-level cloud under mid-level cloud. By design, this technique increases the low-level cloud cover across West Africa, with about a 10% increase in SWA. Results using this statistical method, as well as its skill, will be evaluated against SYNOP observations (Van der Linden et al., 2015).

3.1.2 Aerosol

Figure 3 shows mean aerosol optical depths (AOD) at 550 nm from MODIS, and mean differences between MODIS and SEAWIFS and MISR (note that the MISR AOD is at 555 nm). AOD is only retrieved in clear-sky conditions, resulting in relatively few retrievals in the cloudy region near the gulf of Guinea. Even over clear-sky regions and despite SeaWiFS and MODIS using the same deep blue aerosol optical depth retrieval algorithm over land, the three products show substantial differences. AOD is largest over the Sahara due to dust. Larger AOD values can also be observed to the south due to biomass burning. Over ocean, both SeaWiFS and MISR generally show lower AODs than MODIS. Over land, the differences between MODIS and both MISR and SeaWiFS show a meridional pattern, but in opposite directions.

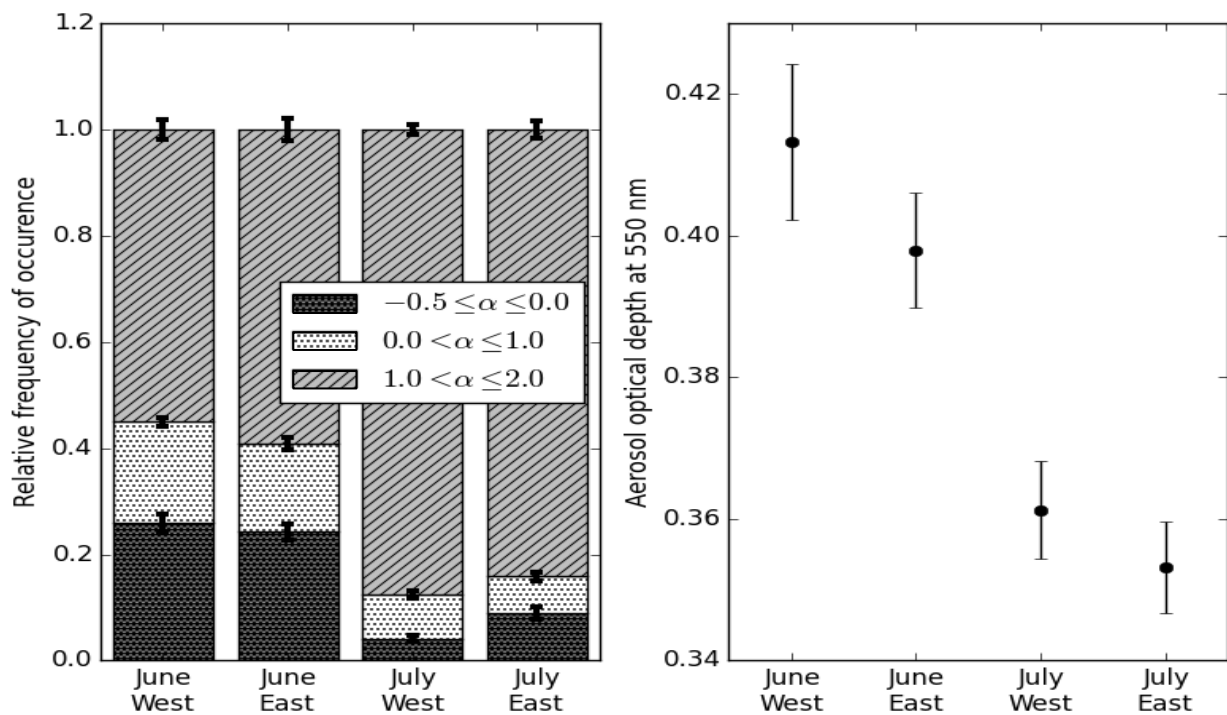


Figure 4. Left: Relative frequency of occurrence of different Ångström Exponents for MODIS AOD retrievals in the West and East sub-domains, for June and July. Right: Mean MODIS AOD for the West and East sub-domains, June and July.

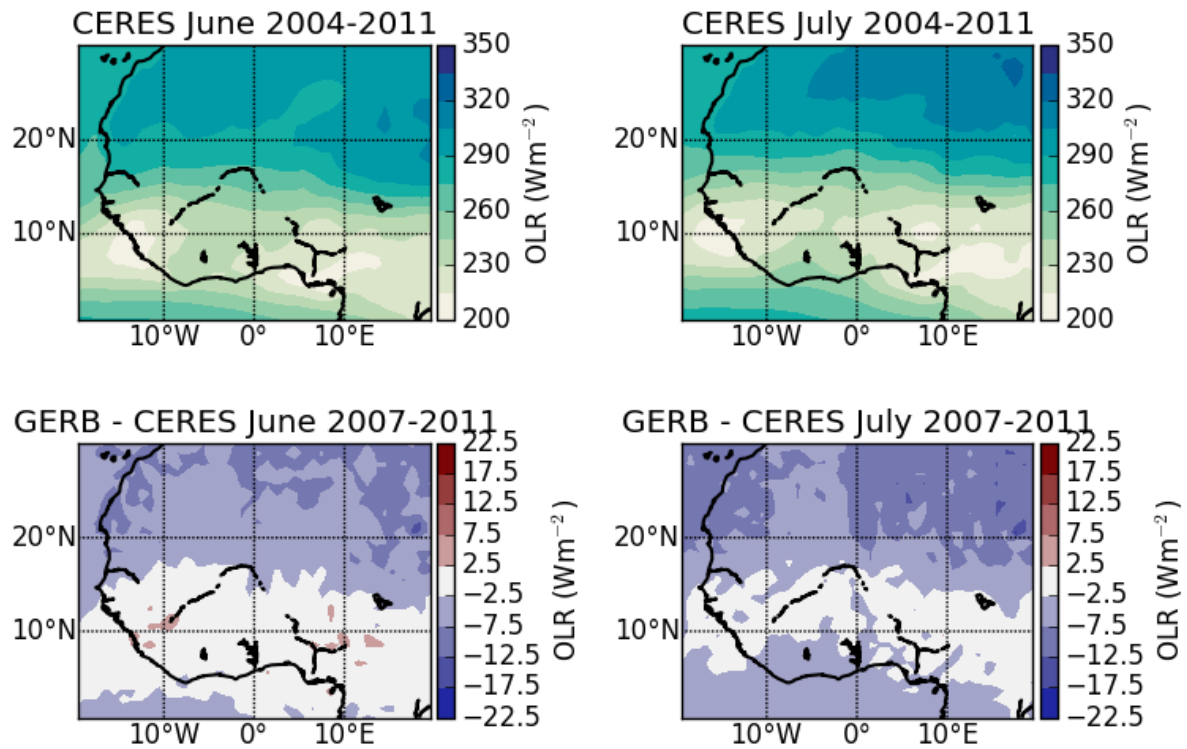


Figure 5. Multi-annual (2004-2011) climatologies of outgoing LW radiation for June (left) and July (right). Top row shows values from CERES, bottom row shows differences between CERES and GERB.

Alongside the AOD, MODIS also estimates an Ångström exponent (α) for each clear-sky point. Figure 4 shows relative frequency of occurrence of these Ångström exponents for the two sub-domains together with mean AODs. The AOD is slightly larger in the West, but the distribution of Ångström exponents is similar between the two sub-domains with fine mode particles ($\alpha > 1$) dominant. Both sub-domains show a decrease in AOD from June to July, while the relative frequency of fine mode particles increases from 55-60% to 80-90%, replacing occurrence of coarse mode dust particles ($\alpha \leq 1$).

3.1.3 Radiative fluxes

Figure 5 shows the mean outgoing LW radiation (OLR) at the top of atmosphere from CERES between 2004 and 2011 and the difference between CERES and GERB for 2007-2011. OLR is high to the north due to predominant clear skies and low to the south, with the lowest values collocated with the most extensive high-cloud cover (see Figure 1). GERB shows lower OLR than CERES over clear-sky regions, with differences generally less than 10 W m^{-2} and never exceeding 20 W m^{-2} . Differences between GERB and CERES are much smaller in cloudy regions, with broad areas where the differences are less than 2.5 W m^{-2} . Differences are generally larger in July than June.

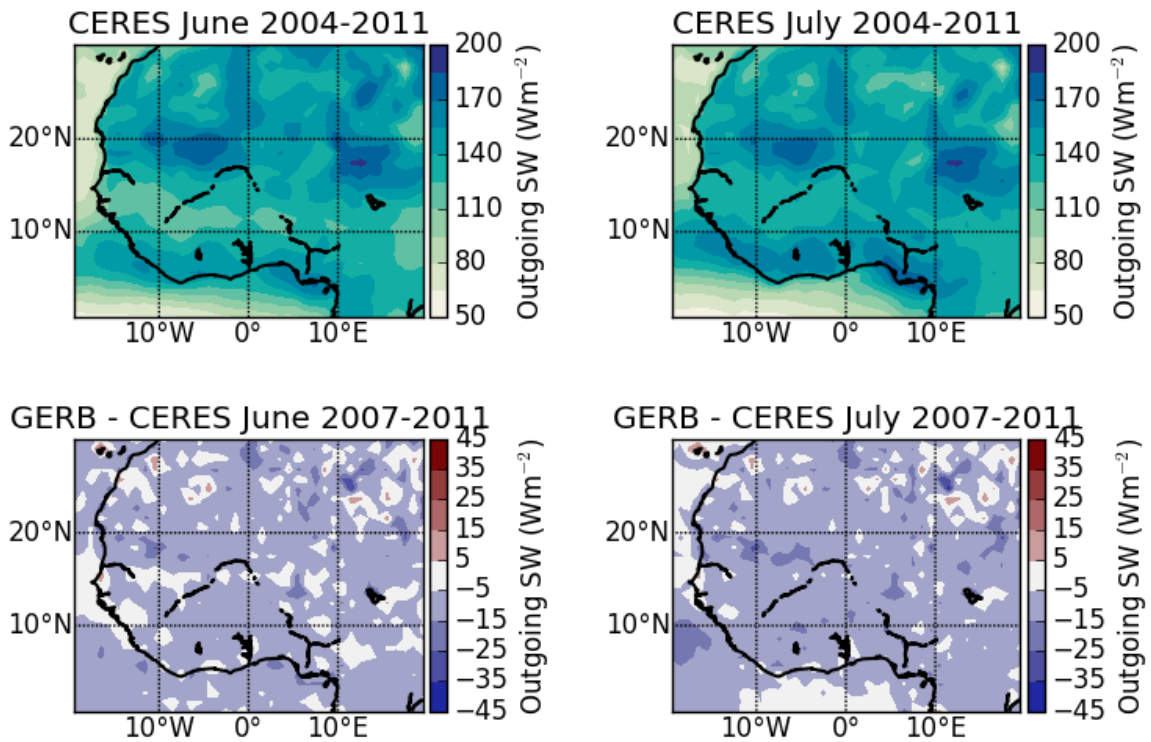


Figure 6. Multi-annual (2004-2011) climatologies of outgoing SW flux for June (left) and July (right). Top row shows means from CERES-EBAF. Bottom row shows differences between CERES and GERB for 2007-2011.

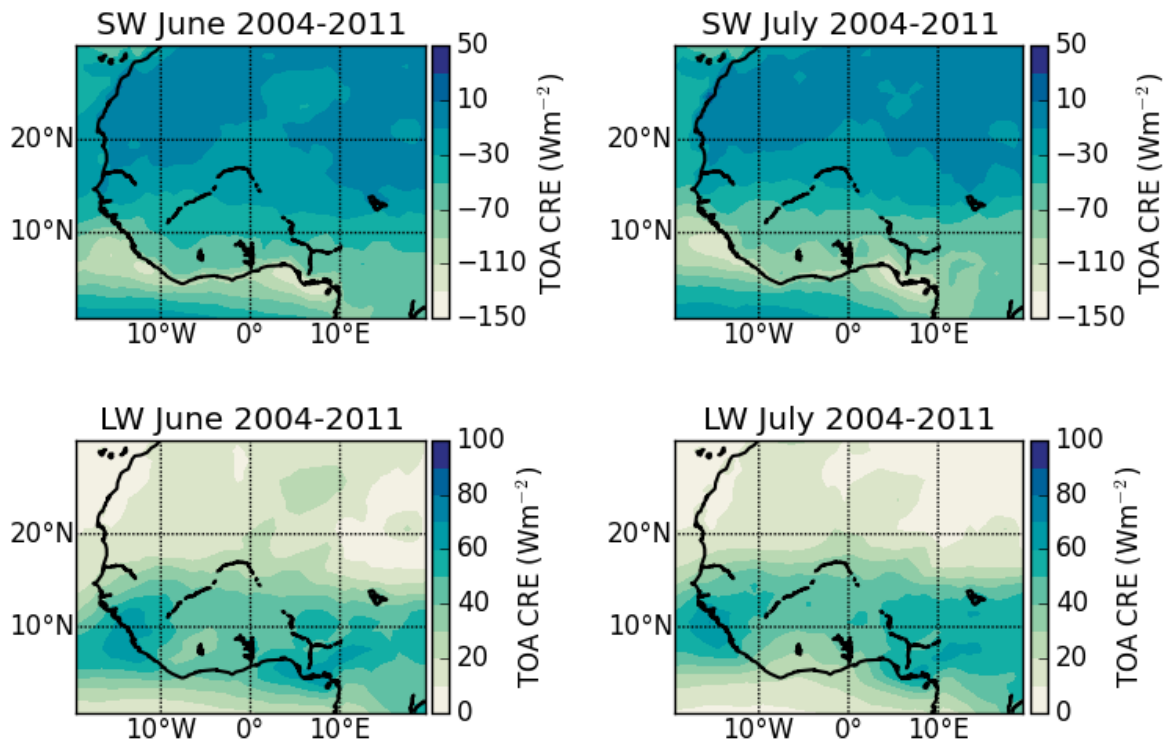


Figure 7. Multi-annual (2004-2011) top of atmosphere cloud radiative effect for June (left) and July (right) from CERES. Top row shows SW and bottom row shows LW.

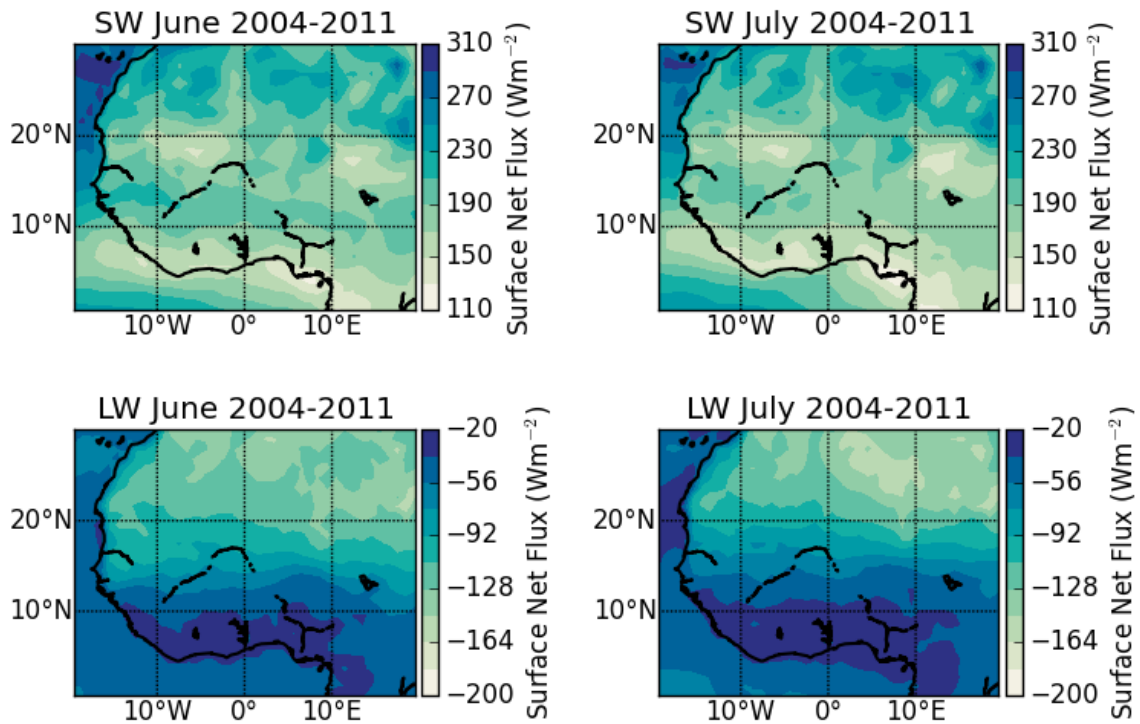


Figure 8. Multi-annual (2004-2011) surface net downwards flux from CERES for June (left) and July (right). The top row shows SW flux and the bottom row shows LW.

Figure 6 shows CERES mean outgoing SW fluxes between 2004 and 2011 and differences between CERES and GERB for 2007-2011. The outgoing SW shows a clear-split between land and ocean due to the surface albedo differences. While there is a clear signal in the outgoing SW flux from clouds over the ocean, the high land surface albedo makes it much harder to identify cloudy regions over land. Bright desert surfaces show up as regions of high outgoing SW fluxes, for instances at (5°W, 19°N) and (12°E, 17°N). GERB outgoing SW fluxes are 5-15 $W m^{-2}$ lower than CERES retrievals throughout much of the region (Fig. 6).

Figure 7 shows CERES EBAF TOA cloud radiative effect (CRE). In both the SW and LW, the CRE is smaller in magnitude north of 15°N, where Figure 1 shows little cloud, and larger towards the south where cloud is more common. The LW CRE pattern is very similar to that for high cloud shown in Figure 1 and many of the high cloud fraction differences between June and July are evident in the LW CRE. The midlevel cloud shown in Figure 1 has a clear signal in the LW CRE to the north of the domain. The SW pattern is very similar to the LW. The main difference being larger SW CRE values over the oceans due to low clouds.

Figure 8 shows surface net downwards fluxes from CERES. In the LW, the net flux magnitude is largest to the north where there is reduced atmospheric emissivity due to fewer clouds and lower humidity. Smallest values occur where there is greater cloud cover and higher humidity along the coast of the gulf of Guinea. Generally the pattern looks similar to the sum of the low, mid-level and high cloud cover in Figure 1. In the SW, the pattern is again due to a combination of cloud cover and surface albedo. The net flux is largest in the north-west corner of the domain. This suggests that the corresponding low cloud shown in Figure 1 is very thin.

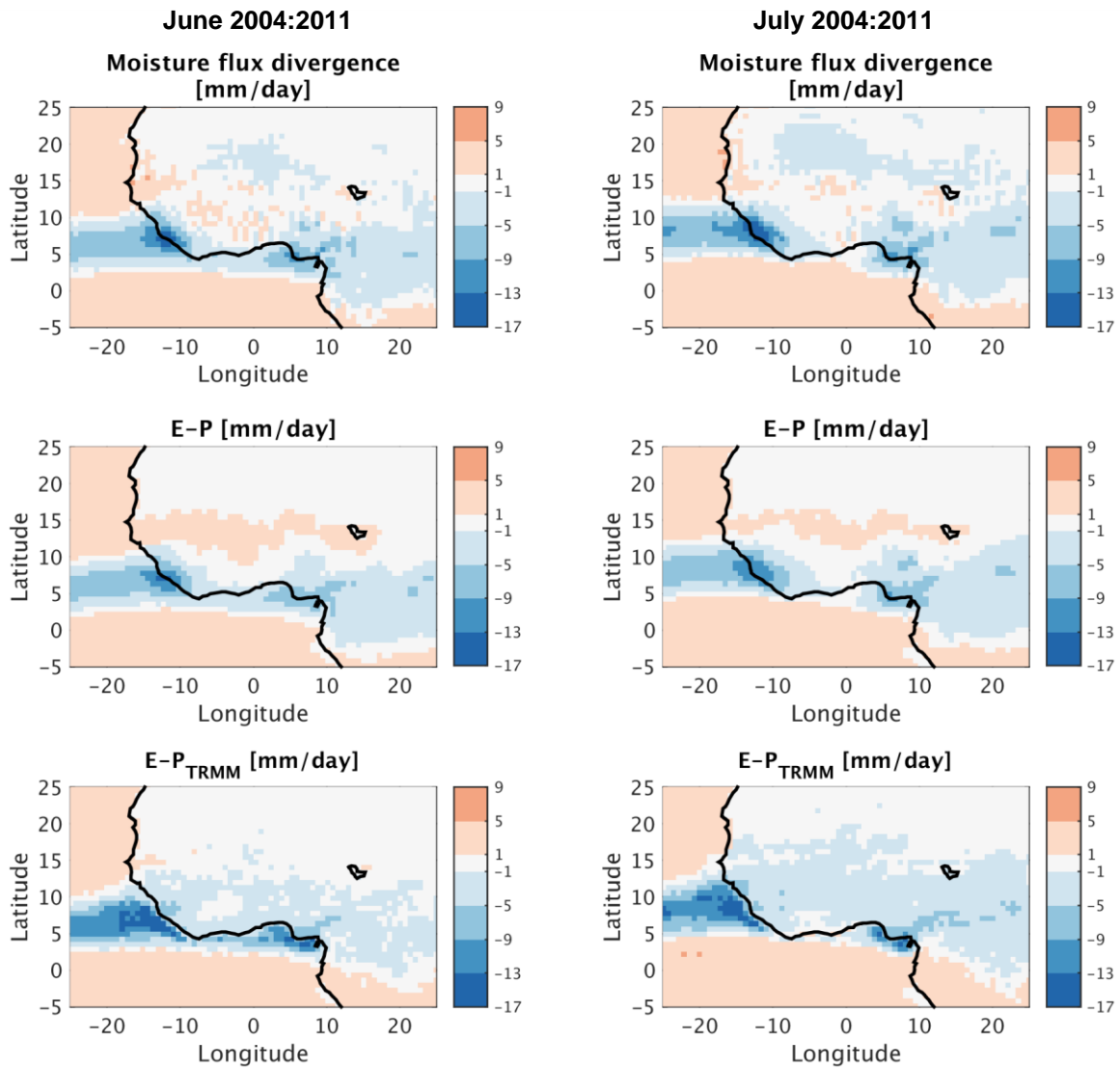


Figure 9. Moisture budget values for 2004-2011, calculated from ERA-Interim re-analyses. Top: moisture flux divergence, negative (blue) values indicate moisture convergence. Middle: E-P from re-analyses data only. Bottom: E-P, with P taken from TRMM observations. Left: June, Right: July.

3.1.4 Moisture budget

In Figure 9, we show the moisture flux divergence, as well as E-P (evaporation minus precipitation) from the ERA-Interim reanalyses for the period 2004-2011. We use the convention that negative values (in blue in Figure 9) show moisture convergence. The differences between the moisture flux divergence and E-P are small. The region of moisture convergence coincides with the region of highest average rainfall and highest high-level fractional cloud cover. Moisture convergence increases from June to July over Benin while decreasing over the coastal regions of Ghana. Interestingly, the mid-level cloud cover over the Sahel and Sahara largely coincides with the (small) moisture flux convergence in this region. The band of positive P-E around 10°-15°N in ERA Interim is explained by unrealistic positioning of the intertropical convergence zone based upon comparison with TRMM precipitation and comparison of ERA Interim cloud with observations.

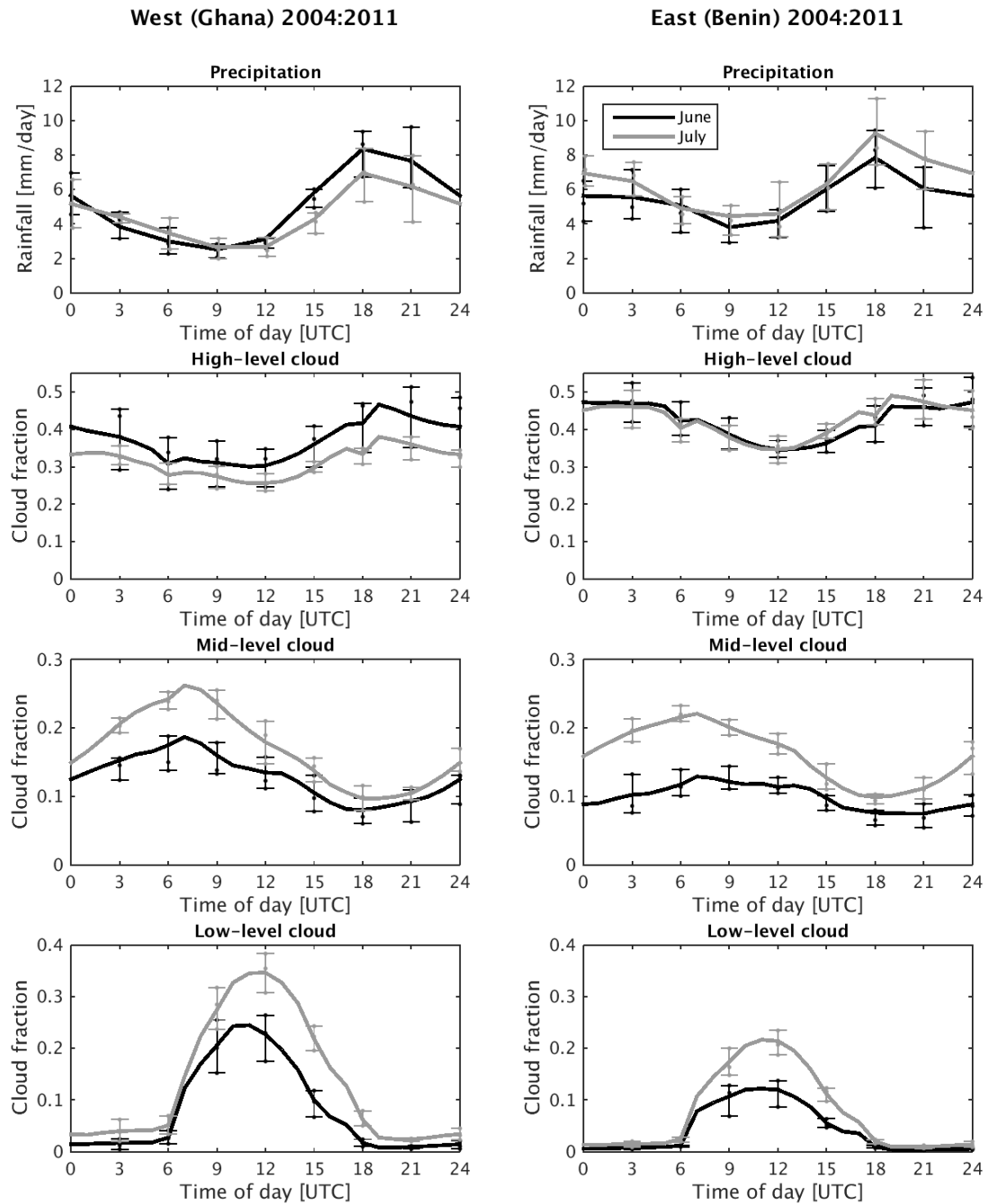


Figure 10. Mean diurnal cycle for the two subdomains, Ghana/west (left) and Benin/east (right), for June (black) and July (grey) 2004-2011. First row: rainfall from TRMM. Second row: high-level cloud cover from CM-SAF. Third row: mid-level cloud cover from CM-SAF. Fourth row: low-level cloud cover from CM-SAF.

3.2 Diurnal cycle

We now consider the climatological mean diurnal cycle for multiple variables over the two regions marked as boxes in Figure 1, referred to as Benin (east) and Ghana (west).

3.2.1 Clouds and precipitation

The diurnal cycles for the two subdomains (Figure 10) are approximately in phase, with maximum low-level cloud cover around 10-11 UTC (in agreement with Van der Linden et al. (2015)) and maximum rainfall around 18 UTC. Low-level cloud fraction in the west subdomain is a factor 2

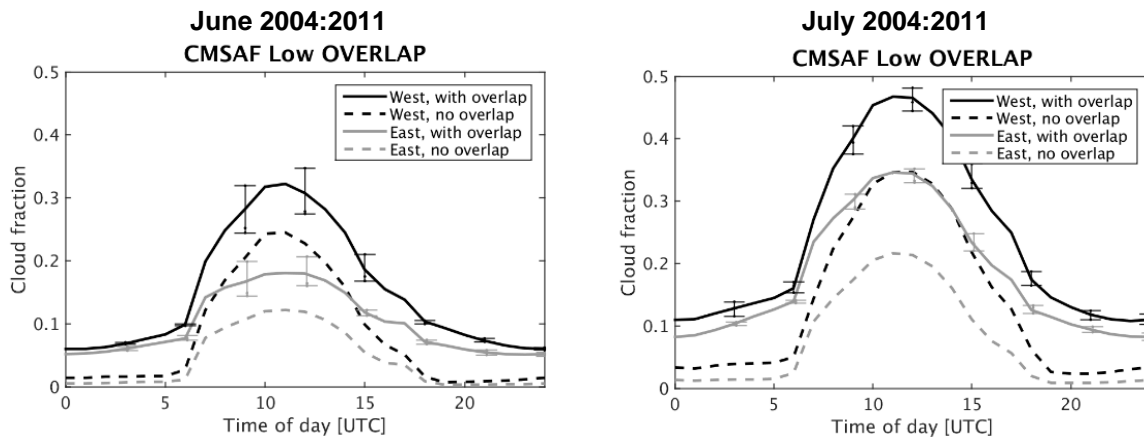


Figure 11. Diurnal cycle of low-level cloud cover derived from CM-SAF but adjusted with CloudSat-CALIPSO overlap statistics, assuming an overlap probability fitted to a sinusoid with maximum at 11 UTC and minimum at 23 UTC. Left: June, right: July.

greater than in the east, while in both subdomains the low-level cloud fraction is greater in July than in June. In the west, this may be partly due to greater high-level cloud cover in June than in July. There is little or no low-level cloud cover after 18 UTC or before 6 UTC, which is due to known limitations of the CMSAF product (section 3.2). Van der Linden et al. (2015) complement the CMSAF product with separate low-level cloud retrievals from SEVIRI measurements using the red-green-blue composites “nighttime microphysical scheme” (Lensky and Rosenfeld, 2008). Using this product, Van der Linden et al. (2015) report seasonal mean low-level cloud cover at 24 UTC of approximately 0.2 in the West subdomain and 0.1 in the East.

The diurnal cycle of high-level cloud is possibly slightly lagged compared to the diurnal cycle of precipitation, with a minimum around 12 UTC. High-level cloud cover does not decrease as strongly from 18 UTC onwards, however, and especially in the east, the diurnal variation is small. For both subdomains, mid-level cloud cover is highest at 7 UTC and lowest at 18 UTC and it is 5–10% greater in July than in June. The morning maximum of mid-level cloud cover could be due to remnants of convection, e.g. descending cirrostratus or mid-level outflow.

When we adjust the low-level cloud cover with the CloudSat-CALIPSO overlap statistics we see an overall increase of about 5% in June and 10% in July (Figure 11). Although the phase of the diurnal cycle agrees with Van der Linden et al. (2015), the cover is less than what they derived from SYNOP observations and less than derived using the nighttime RGB composite technique.

3.2.2 Frequency of cloud occurrence

In Figure 12 we show the diurnal cycle of frequency of significant cloud cover for 0.2 and 0.6 cloud fraction. When individual hourly SEVIRI observations indicate cloud fraction above a specific threshold (0.2 or 0.6) for a 0.25° by 0.25° area, this is registered as “cloud occurrence”; what is shown in Figure 12 is the frequency of such events for June and July, averaged over each of the two subdomains. The two thresholds indicate different diurnal cycles, possibly because a cloud fraction of 0.2 could be due to widespread broken-up cumulus as well as stratus, while a cloud fraction above 0.6 indicates stratus only.

Stratus (fraction above 0.6) peaks at 10–11 UTC in both months and in both locations, occurring twice as frequent in the West than in the East. The occurrence of low-level cloud fractions above 0.2 peaks at 12 UTC in both locations and remains above 0.1 until 15 UTC, whereas stratus

frequency decreases sharply after 12 UTC. These frequencies will be affected by (partial) high- and mid-level cloud cover, requiring further analysis using CloudSat-CALIPSO overlap statistics and verification against SYNOP observations.

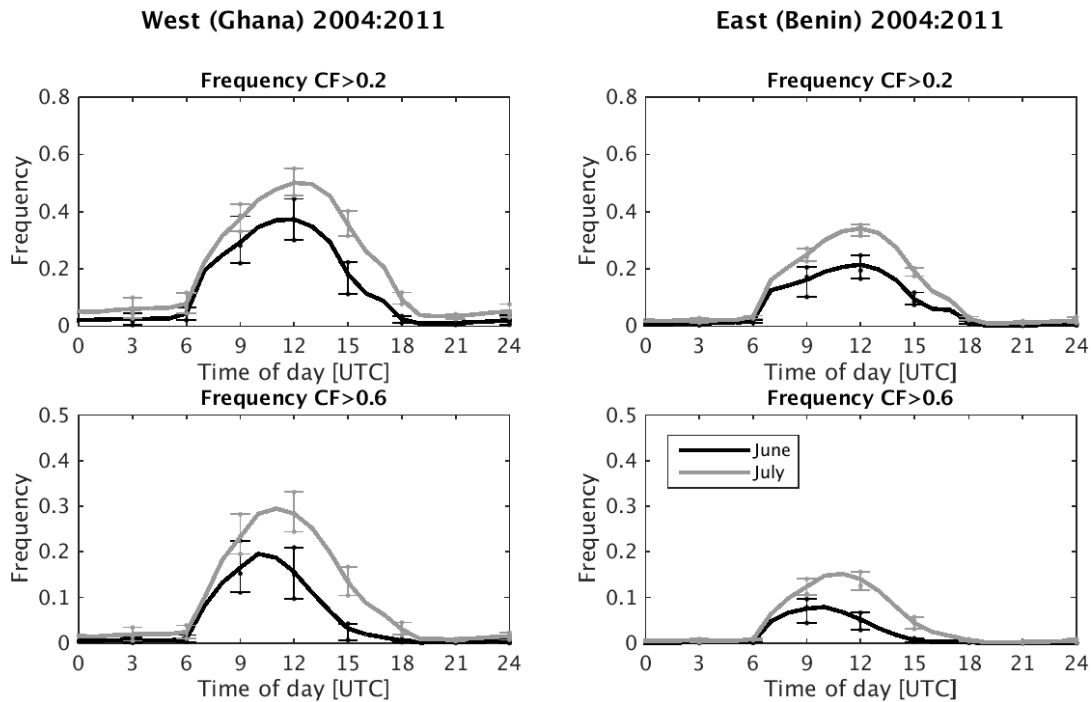


Figure 12. Diurnal cycle of low-level cloud frequency of occurrence for June (black) and July (grey), for West (left) and East (right) sub-domains. Top row shows occurrence of cloud fraction above 0.2 and bottom row above 0.6.

3.2.3 Radiative fluxes

Figure 13 shows the diurnal cycle of TOA outgoing shortwave and longwave radiation from GERB. Both subdomains show a clear diurnal cycle in TOA OLR in June, during the pre-onset period when the West Africa rainfall maximum is still partly over the ocean and along the Guinean coast. There is a slight difference between the West and East subdomains in the early mornings, which may be due to propagating convection overnight through the East domain causing lower OLR, while this doesn't reach the West domain. In July, the diurnal cycle is less pronounced, although both subdomains still have their lowest OLR in the early morning (4 UTC), at slightly lower values than in June, and highest in the mid-to-late afternoon. The East subdomain has generally 10 W m^{-2} lower OLR than the West in July, likely as it is closer to the convectively active regions of SE Nigeria and the Cameroon Highlands. The outgoing SW shows slight differences between the East and West subdomains, too. The West subdomain has generally higher SW fluxes.

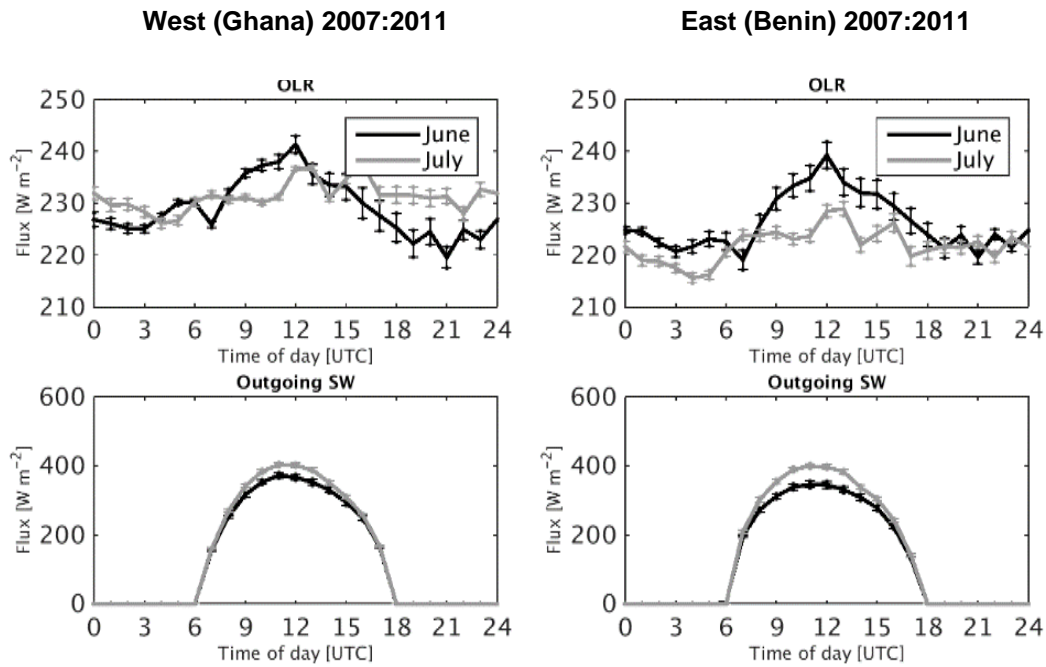


Figure 13. Mean diurnal cycle for the two subdomains, Ghana/west (left) and Benin/east (right), for June (black) and July (grey) 2007-2011. First row: TOA OLR from GERB. Bottom row: TOA SW fluxes from GERB.

3.3 Interannual variability

3.3.1 Clouds and precipitation

Both subdomains experience large year-to-year variations of rainfall ranging from around 3 to 8 mm day⁻¹ in the West subdomain and 4 to 9 mm/day in the East (Fig. 14). From the climatology, we might expect that the monthly rainfall is correlated with high-level cloud cover, but over the eight years, no significant correlations were found for either of the subdomains. Nevertheless, the results suggest that there is more high-level cloud cover in years with higher rainfall.

High-level cloud cover ranges from around 20-40% in the West subdomain and 30-50% in the East subdomain. Mid-level cloud exhibits less year-to-year variability, apart from a maximum extent in both subdomains for June 2004. Mid-level cloud cover in the West subdomain ranges from about 10-20% and 7-19% in the East subdomain. For both subdomains, in July mid-level cloud cover is greater than in June.

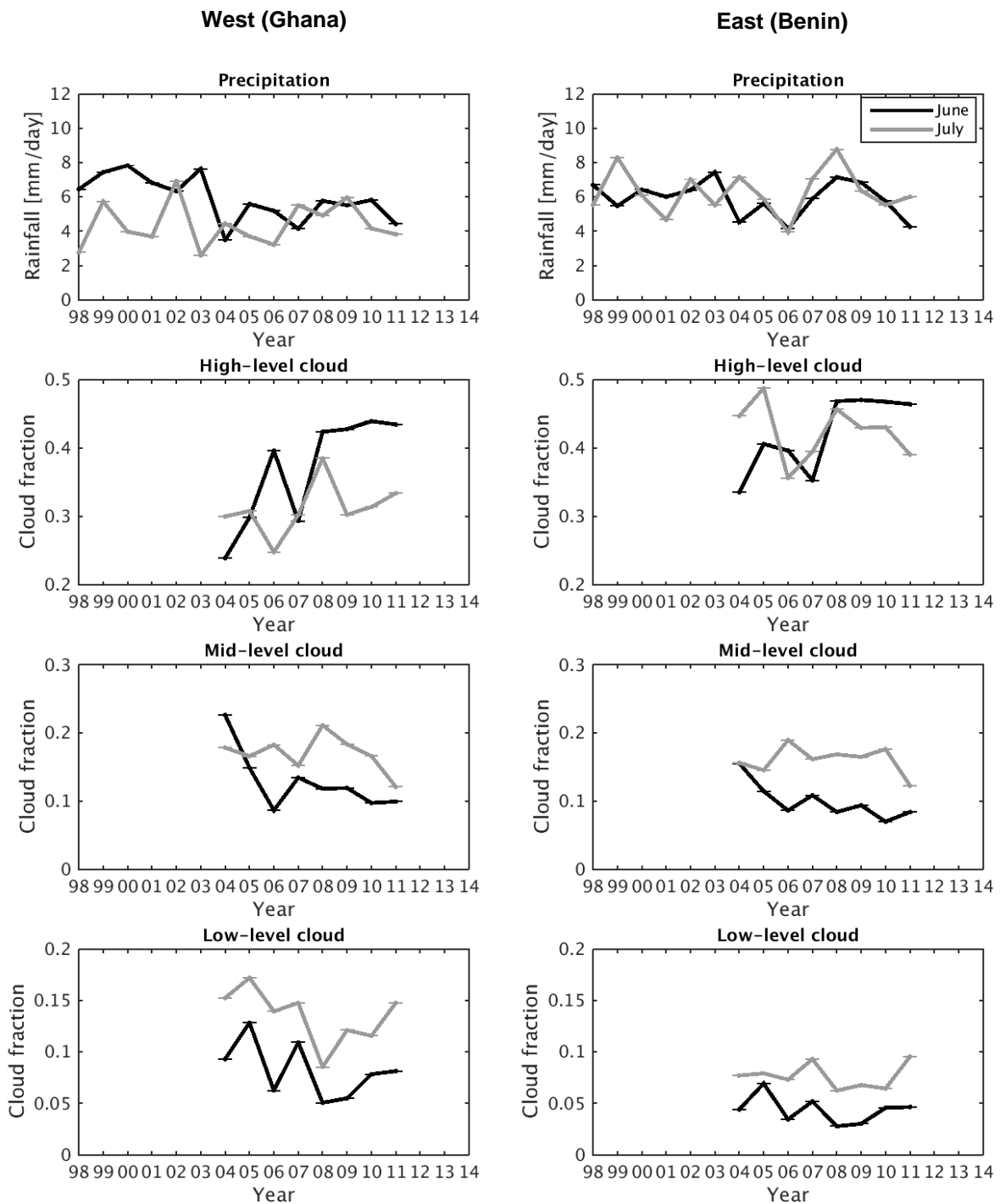


Figure 14. Interannual variability for the two subdomains, Ghana/west (left) and Benin/east (right), for June (black) and July (grey) 2004-2011. First row: rainfall from TRMM. Second row: high-level cloud cover from CM-SAF. Third row: mid-level cloud cover from CM-SAF. Fourth row: low-level cloud cover from CM-SAF.

Low-level cloud cover has greater year-to-year variability in the West subdomain than in the east, though it also has a higher mean. The ranges are 5-13% for June in the West and 9-17% for July; in the East, the ranges are 3-7% and 6-10% respectively. Interestingly, for both subdomains, the June and July means appear correlated, suggesting that low-level cloud cover could be dominated by large-scale or global temperature and circulation patterns.

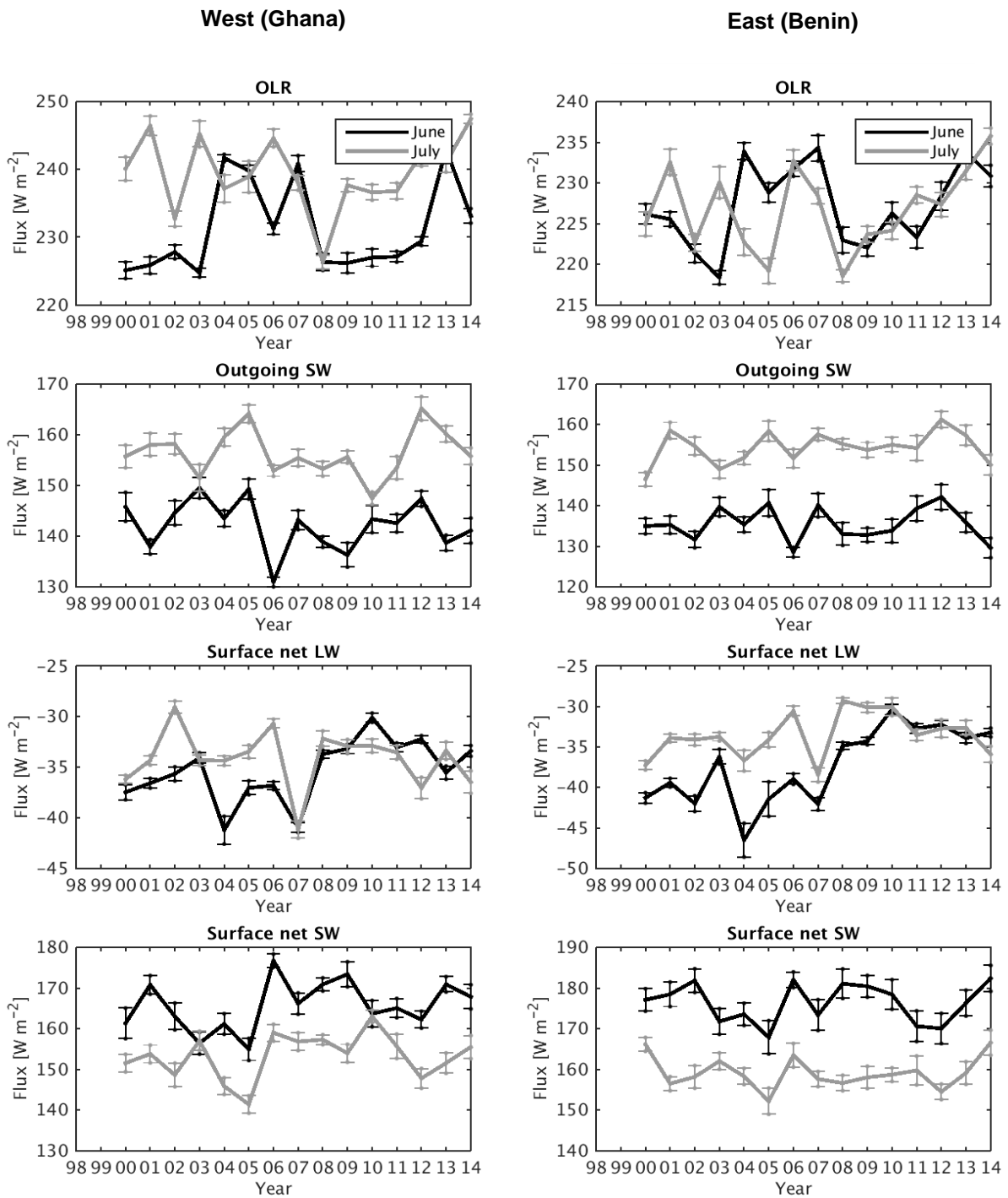


Figure 15. As Figure 14, but for TOA fluxes from CERES (first and second row) and mean surface net fluxes (third and fourth rows).

3.3.2 Radiative fluxes

During the period 2004-2007 OLR is elevated by around 10 W m⁻² in June over both east and west sub-domains and is associated with reduced upper level cloud cover and generally lower precipitation (Fig. 15). There is a trend towards reduced surface longwave cooling in June over the CERES period. There a systematic decrease of around 10-20 W m⁻² in SW absorbed at the surface from June to July which is consistent with the larger fraction of low and mid-level cloud and of larger magnitude than the year to year variability shown for each month.

4 Summary and key findings

A multi-dataset evaluation of clouds, radiation, aerosol and precipitation is conducted over the southern West Africa region to provide context and outline the primary datasets for use within the DACCIWA work program. The principle initial findings are as follows:

- 1) There is good agreement between GERB and CERES estimates of top of atmosphere radiative energy fluxes which increases confidence in their use to understand cloud radiative processes although systematic differences in SW radiative fluxes of around $5\text{-}10\text{ Wm}^{-2}$ are close to their expected monthly mean uncertainty.
- 2) There are considerable differences between standard aerosol satellite climatologies which should be understood in more detail.
- 3) Obscuring of low clouds by mid and high-level clouds in the satellite view requires a strategy for correcting of low cloud fractions.
- 4) There is an increase in mid and low-level cloud fraction from June to July of approximately 5% (depending upon region) with consequent decreased surface SW radiation.
- 5) The diurnal cycle of high-level cloud is in phase with the diurnal cycle of precipitation, with a minimum around 12 UTC. Mid-level cloud shows a contrasting diurnal cycle, peaking at 7 UTC and with lowest mid-level cloud fraction at 18 UTC
- 6) The diurnal cycle in low level cloud fraction is pronounced, peaking at around 11 UTC in agreement with previous work (e.g. van der Linden et al. 2015).
- 7) Frequency of occurrence of high low-level cloud fraction events such as stratus (fraction above 0.6) occur more often in July than in June and occur most frequently around 10 UTC.
- 8) High-level cloud cover ranges from around 20-40% in the west subdomain and 30-50% in the east. The 2004-2007 period exhibit less high cloud fraction and higher outgoing longwave radiation than following years.
- 9) There is consistency between spatial patterns in rainfall, high-level cloud and outgoing longwave radiation and cloud radiative effect.
- 10) Both subdomains experience large year-to-year variations of rainfall ranging from around 3 to 8 mm day^{-1} in the West subdomain and 4 to 9 mm day^{-1} in the East.
- 11) There is qualitative consistency between ERA Interim moisture convergence and precipitation minus evaporation (P-E); better agreement is produced when replacing ERA Interim P with TRMM data and this approach is therefore recommended.

5 References

CERES Science Team, Hampton, VA, USA: NASA Atmospheric Science Data Center (ASDC), Accessed 30 April 2014 at doi: 10.5067/Terra/CERES/EBAF-TOA_L3.002.8

CERES Science Team, Hampton, VA, USA: NASA Atmospheric Science Data Center (ASDC), Accessed 5 May 2015 at doi: 10.5067/Terra/CERES/EBAF-SURFACE_L3.002.8

DeWitte, S., Gonzalez, L., Clerbaux, N., Ipe, A., Bertrand, C., & De Paepe, B., 2008: The geostationary earth radiation budget edition 1 data processing algorithms. *Advances in Space Research*, 41(11), 1906-1913.

Harries, J. E., J. E. Russell, J.A. Hanafin, H. Brindley, J. Futyran, J. Rufus, S. Kellock, G. Matthews, R. Wrigley, A. Last, J. Mueller, R. Mossavati, J. Ashmall, E. Sawyer, D. Parker, M. Caldwell, P. M. Allan, A. Smith, M. J. Bates, B. Coan, B. C. Stewart, D. R. Lepine, L. A. Cornwall, D. R. Corney, M. J. Ricketts, D. Drummond, D. Smart, R. Cutler, S. Dewitte, N. Clerbaux, L. Gonzalez, A. Ipe, C. Bertrand, A. Joukoff, D. Crommelynck, N. Nelms, D. T. Llewellyn-Johnes, G. Butcher, G. L. Smith, Z. P. Szewczyk, P. E. Mlynchak, A. Slingo, R. P. Allan and M. A. Ringer, 2005: The Geostationary Earth Radiation Budget Project. *Bulletin of the American Meteorological Society*, Volume 86, No. 7, pp 945-960.

Huffman, George J., David T. Bolvin, Eric J. Nelkin, David B. Wolff, Robert F. Adler, Guojun Gu, Yang Hong, Kenneth P. Bowman, and Erich F. Stocker, 2007: The TRMM Multisatellite Precipitation Analysis (TMPA): Quasi-Global, Multiyear, Combined-Sensor Precipitation Estimates at Fine Scales. *J. Hydrometeor*, 8, 38–55.

Hsu, N. C. M.-Jeong, C. Bettenhausen, A. M. Sayer, R. Hansell, C. S. Seftor, J. Huang, and S.-C. Tsay, 2013a: Enhanced Deep Blue Aerosol Retrieval Algorithm: the 2nd Generation, *J. Geophys. Res.*, doi: 10.1002/jgrd.50712 (accepted)

Knippertz, P., A. H. Fink, R. Schuster, J. Trentmann, J. M. Schrage, and C. Yorke, 2011: Ultra-low clouds over the southern West African monsoon region, *Geophys. Res. Lett.*, 38, L21808.

Liebmann, B., I. Blade, G. N. Kiladis, L. M. Carvalho, G. B. Senay, D. Allured, S. Leroux, and C. Funk, 2012: Seasonality of African precipitation from 1996 to 2009. *Journal of Climate*, 25, 4304-4322.

Lensky, I. M. and Rosenfeld, D., 2008: Clouds-Aerosols-Precipitation Satellite Analysis Tool (CAPSAT), *Atmos. Chem. Phys.*, 8, 6739-6753.

Levy, R. C., Mattoo, S., Munchak, L. A., Remer, L. A., Sayer, A. M., Patadia, F., and Hsu, N. C., 2013: The Collection 6 MODIS aerosol products over land and ocean, *Atmos. Meas. Tech.*, 6, 2989-3034, doi:10.5194/amt-6-2989-2013.

Loeb, Norman G., Bruce A. Wielicki, David R. Doelling, G. Louis Smith, Dennis F. Keyes, Seiji Kato, Natividad Manalo-Smith, and Takmeng Wong, 2009: Toward Optimal Closure of the Earth's Top-of-Atmosphere Radiation Budget. *J. Climate*, 22, 748-766. doi: <http://dx.doi.org/10.1175/2008JCLI2637.1>

MISR Science Team, Terra/MISR Level 3, Component Global Aerosol Monthly, version 4, Hampton, VA, USA: NASA Atmospheric Science Data Center (ASDC), Accessed 17 June 2015 at doi: 10.5067/Terra/MISR/MIL3MAE_L3.004

Nguyen, H., Thorncroft, C. D. and Zhang, C., 2011: Guinean coastal rainfall of the West African Monsoon. *Q.J.R. Meteorol. Soc.*, 137: 1828–1840. doi: 10.1002/qj.867

Sayer, A. M., N. C. Hsu, C. Bettenhausen, Z. Ahmad, B. N. Holben, A. Smirnov, G. E. Thomas, and J. Zhang, 2012: SeaWiFS Ocean Aerosol Retrieval (SOAR): Algorithm, validation, and comparison with other data sets, *J. Geophys. Res.*, 117, D03206, doi:10.1029/2011JD016599

SeaWiFS (Sea-Viewing Wide Field-of-View Sensor): N. Christina Hsu, Andrew M. Sayer, M.-J. Jeong, and Corey Bettenhausen: SeaWiFS Deep Blue Aerosol Optical Depth and Angstrom Exponent Monthly Level 3 Data Gridded at 1.0 Degrees, version 004, Greenbelt, MD, USA: Goddard Space Flight Center Distributed Active Archive Center (GSFC DAAC), Accessed 15 June 2015 at doi:10.5067/MEASURES/SWDB/DATA304

Stengel, M., Kniffka, A., Meirink, J. F., Lockhoff, M., Tan, J., and Hollmann, R., 2014: CLAAS: the CM SAF cloud property data set using SEVIRI, *Atmos. Chem. Phys.*, 14, 4297-4311, doi:10.5194/acp-14-4297-2014.

Sultan, Benjamin and Serge Janicot, 2003: The West African Monsoon Dynamics. Part II: The “Preonset” and “Onset” of the Summer Monsoon. *J. Climate*, **16**, 3407–3427.

Van der Linden, R., A. H. Fink, and R. Redl, 2015: Satellite-based climatology of low-level continental clouds in southern West Africa during the summer monsoon season, *J. Geophys. Res. Atmos.*, 120, 1186–1201, doi:10.1002/2014JD022614.